2026 IEEE International Conference on Robotics and Automation (ICRA 2026)
June 1-5, 2026. Vienna, Austria

Simplified fabrication and open-loop control of an electromagnetic insect-scale terrestrial robot

Julie Villamil[1], Yaochen Li[1], Jack Long[2], Michael Karpelson[3], E. Farrell Helbling[1]

***Abstract*— Small-scale terrestrial robots have a number of applications where operation in confined spaces is required. Because of their low mass (less than five grams) and small size (less than five centimeters), their mechanical design requires careful analysis of multiple subsystems (e.g., actuation, power, fabrication, and assembly). Planar electromagnetic actuators show linear force-displacement behavior, large displacements, and low-voltage operation. Here, we integrate these actuators into the Cornell Micro Terrestrial Robot (COMT), a $1.9-\mathrm{g}$ quadrupedal robot that uses a simplified fabrication strategy for the transmissions that takes advantage of the large displacement. Each leg is fabricated using laminate-based techniques, but requires only a single manual fold-and-lock step. The robot ($\mathrm{BL}=3$ cm) achieves speeds up to 4.36 BL/s and consumes approximately 370 mA during operation. These results provide a path towards a untethered terrestrial robots that can navigate in confined spaces and enable future collectives through simplified manufacturing strategies.**

I. Introduction

Small, autonomous legged robotic platforms have been in development for multiple decades for use in inspection of human-unreachable environments. Because of their small size, these cm-scale robots present a number of engineering challenges in the design, manufacturing, and autonomous locomotion of the vehicle [1]. Laminate-based manufacturing (i.e., PC-MEMS [2]) is the most common method for small-scale crawling robots due to the high strength-to-weight ratios of the laminate materials [3]–[5]. However, this process often involves manual fold steps, which limits experimental validation, as robots are difficult to manufacture, and reliability, as robots have varying baseline operating conditions.

Compounding fabrication complexity is the use of high power-density piezoelectric bimorph actuators [4], [5], which require transmission mechanisms to amplify the relatively small displacements ($\sim 100-300$ µm at ~ 200 V) [6]. Additionally, these actuators require high-voltage step up converters [4], [7] for untethered operation, which can reduce system efficiency. Shape memory alloys [8], [9], which have high displacements, are sensitive to temperature fluctuations, require high currents, and cannot be operated at the high frequencies necessary for efficient operation at small scales. Voice coil actuators (VCAs), which use the Lorentz force produced by a current-carrying coil traveling through a permanent magnetic field, can achieve high precision displacement and high force output at low voltages ($d \sim 1-4$ mm, $F \sim 10$s mN, 3 V) [10]–[12].

[1]School of Electrical & Computer Engineering, [2]School of Mechanical & Aerospace Engineering, Cornell University, Ithaca, NY 14580. [3] School of Engineering and Applied Sciences, Harvard University, Allston, MA 02134. Contact e-mail farrell@cornell.edu

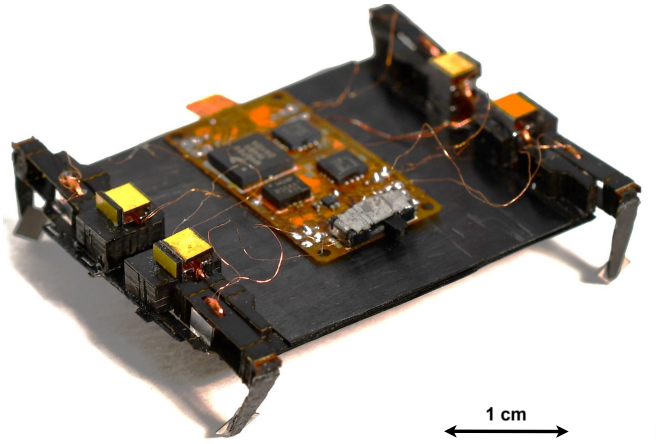

Fig. 1: Cornell Micro Terrestrial Robot. This insect-scale electromagnetically-actuated quadruped uses eight planar voice coil actuators and parallelogram linkages that simplify the cm-scale assembly processes. An onboard circuit board generates open-loop signals to control leg phasing for straight-line and turning trajectories. A lithium-ion battery is mounted underneath the chassis.

The DAWM [10] uses VCAs to deform a lattice of discrete modular components. The robot can generate top speeds of 3.69 cm/s, but the VCAs consume an average current of 600 mA, for an overall cost of transport (COT) of 138. This is defined as the normalized ratio of energy consumption to body mass, gravity, and travel distance [1]. The robot is manually assembled and is currently tethered to offboard power and control. The BHMbot [11] has two active rear legs that are driven by solenoids. Each solenoid consumes 138 mA and requires precise coupling to a four-bar transmission to amplify displacements. The robot can generate high-speeds (35 cm/s), but slows with additional payloads, and has a COT of 237.

In this work, we present the Cornell Micro Terrestrial Robot (COMT), an electromagnetically-driven terrestrial quadruped microrobot (Fig. 1) that can travel at speeds over 12 cm/s (4 BL/s). The actuators consume 46 mA during untethered operation, for a COT of 91. Operating at lower currents increases our total operating range, enabling longer mission times for future untethered deployments. Additionally, our serial transmission mechanism enables a simple manufacturing strategy of laser machining and lamination steps, with only one fold-and-lock step per leg. This fabrication technique will enable future mass production of insect-scale terrestrial robots. The paper is organized as follows: Section II describes the mechanical design and the fabrication process for each leg mechanism; Section III provides details on the design, simulations, and experimental

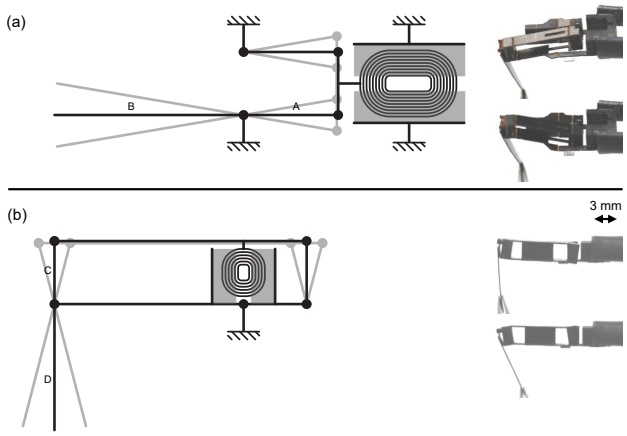

Fig. 2: Schematic of the mechanism and actuator for the lift and swing DOFs of the leg. (a) The lift VCA coil moves through a region of high magnetic field to drive a parallelogram linkage up and down (gray). The vertical output motion is amplified through the transmission at a ratio A:B. (b) The swing VCA coil moves through a region of high magnetic field to drive a parallelogram linkage left and right. The output motion is amplified through the transmission at a ratio C:D. Still images from the manufactured laminate at displacement extremes can be seen on the right.

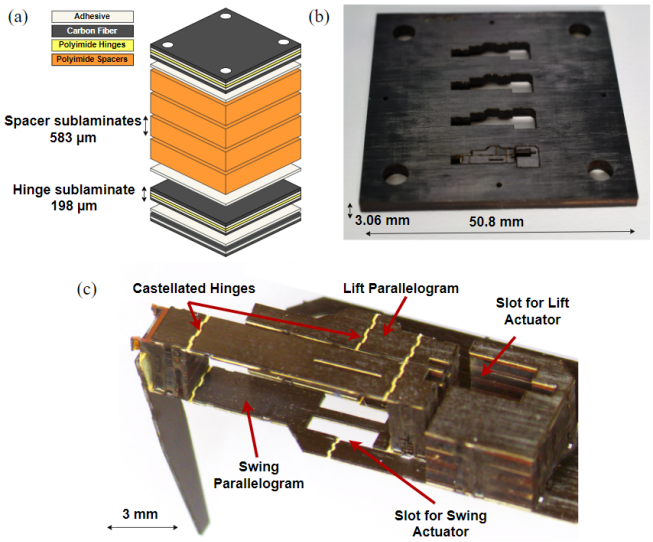

Fig. 3: Simplified fabrication of a single leg mechanism. (a) The single leg is fabricated using a single laminate. This laminate is comprised of four sublaminates: the leg, the bottom hinge layer, the spacer layers, and the top hinge layer (from bottom to top). (b) The laminate is approximately 3.06 mm thick and four legs can be manufactured in a single fabrication run. (c) The fully released leg mechanism after the leg has been folded and locked in place.

validation of the VCAs; Section IV describes the full-robot assembly and the leg phasing to enable straight-line locomotion and heading angle adjustment; and Section V presents the robot's open-loop performance.

II. Mechanical Design

Each leg is driven by two miniature VCAs (lift and swing) that form a serial kinematic chain. Because of the high displacement of the VCA actuators, we can utilize parallelogram linkages that enhance fabrication simplicity. In this design, the mechanism can be manufactured almost entirely using laser machining and lamination steps, with only a single fold-and-lock assembly step to attach the foot. We then introduce the VCAs via pick-and-place through the top and bottom of the laminate.

A. Kinematics

Figure 2(a) shows a simplified schematic of the mechanism and actuator for the lift DOF. A parallelogram linkage constrains a planar coil to move vertically through a region of high magnetic field, which is generated by a magnetic core mounted to the mechanical ground of the robot. One of the parallelogram links forms the horizontal part of the robot's leg (the "femur"). Passing a current through the coil generates an electromagnetic force that may deflect the femur up or down from its neutral position, depending on the direction of the current. The transmission ratio between the actuator displacement and the femur tip is given by the ratio of link A to link B.

Figure 2(b) shows a simplified schematic of the mechanism and actuator for the swing DOF, which is implemented using a second parallelogram linkage forming a kinematic chain with the femur. The magnetic core is mounted to the femur itself, while the planar coil is attached to the link parallel to the femur. To reduce leg inertia, the actuator components are located as close as possible to the femur's axis of rotation; the swing actuator itself is also smaller than the lift actuator as it requires a lower force output. In this case, passing a current through the coil will cause the top link to move laterally with respect to the femur, generating a similar lateral deflection in the foot of the robot. The transmission ratio between the actuator displacement and the foot displacement relative to the femur is given by the ratio of link C to link D.

B. Fabrication

We manufacture the mechanism using a series of laser machining and lamination steps [2]. There are four primary sublaminates: the foot (i.e., link D), the first parallelogram link (i.e., the femur), spacer layers (i.e., link C), and the second parallelogram link. The parallelogram sublaminates are standard castellated hinge layers [3], [13]: five layers of rigid carbon fiber (90 µm carbon fiber, QA112, Toho Tenax), flexible polyimide (12.5 µm), and adhesive (12.5 µm, FR1500, Dupont) materials are pre-patterned using a high-resolution laser cutter (15µm spot size, Protolaser U4, LPKF), pin aligned, and laminated under heat and pressure. To create the spacer layers, we laminate polyimide (127 µm) and adhesive (25.4 µm, FR0100 Dupont) until we reach the desired length for link C. The foot is comprised of two layers of carbon fiber for structural rigidity. As shown in Fig. 3(a), we laminate the four sublaminates into one final single-leg assembly. Given the size of the laminate, we can manufacture multiple legs in a single process (see Fig. 3(b)). We perform release cuts to remove each leg from the surrounding structure. The foot is then manually folded and locked into place. The fully

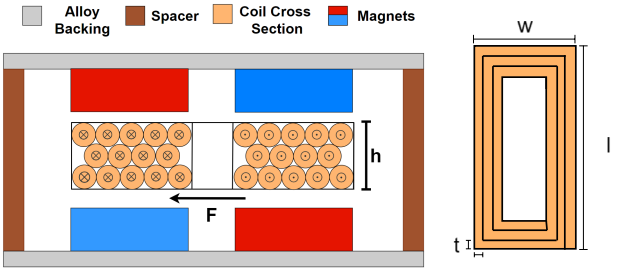

(a) (b)

Fig. 4: Planar Voice Coil Actuator (a) Cross-section of the actuator. The magnetic core is comprised of the alloy backing and the two pairs of permanent magnets. A current-carrying coil in the middle of the magnet core generates a Force F according to the Lorentz force equation. (b) The coil is comprised of many windings of thin wire with a thickness (t), a total length (l) and a total width (w).

assembled structure can be seen in Fig. 3(c) with slots for the lift and swing VCAs.

III. Actuator Design and Characterization

VCAs can be assembled at the mm-scale and have demonstrated sufficient force production and displacements for actuation in cm-scale robots [12], [14]–[16]. While many VCAs use cylindrical designs [17], [18], we use a planar design [19] for ease of integration with the leg laminate described in the previous section. As shown in Fig. 4, these actuators have magnetic core assemblies that are comprised of two pairs of complementary permanent magnets and two pole pieces made of a soft magnetic alloy. A single, planar current-carrying coil of wire moves within the core to generate displacement and two spacer layers maintain structural stability and magnetic separation.

We need to select actuator parameters that maximize force production while maintaining low current for untethered operations. The force produced by the current-carrying coil is described by the Lorentz force law:

$$F = 2NIBL, \tag{1}$$

where I is the current in the coil (A), N is number of coil turns, B is magnetic field intensity (T), and L is length of the wire perpendicular to the magnetic field (m). Thus, to maximize force production, we can increase the number of turns, the current through the wire, the magnetic field strength, or the effective length of the wire under the magnets.

A. Design Specifications

The lift actuators need to support the weight of the robot as well as generate sufficient displacement to lift the leg off of the ground. We selected $1 \times 1 \times 3$ mm^3 magnets (Neodymium 50, M0251, SuperMagnetMan) for the lift actuators, as they meet the size and mass requirements of our system while generating sufficient magnetic field strength. Because of the serial configuration of the linkages, we need to minimize swing actuator mass, which sits in the middle of the femur (see Fig. 3). Thus, we selected $0.5 \times 1 \times 2$ mm^3

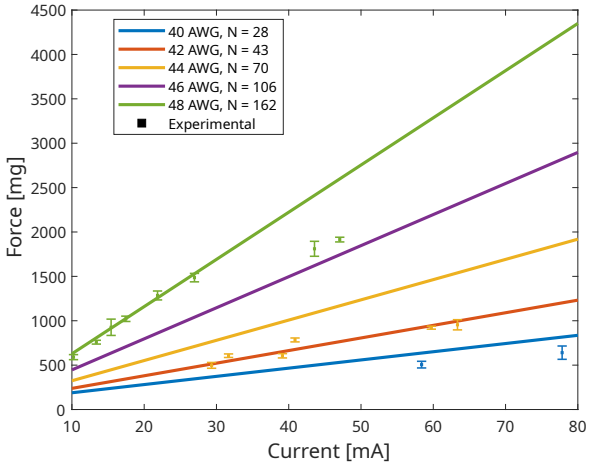

Fig. 5: Simulated Force results for varying wire thicknesses with a 0.3 mm^2 coil cross section. As the wire gauge increases, the number of turns N increases and the generated force increases linearly with current. We experimentally validated the $40, 44, 48$ AWG designs over $n = 4$ trials.

Neodymium magnets for the magnetic core of the swing actuators. We performed ANSYS Maxwell simulations to estimate the magnetic field intensity within complementary magnet pairs. For the lift actuators, at simulated distances greater than 500 µm, the magnetic field strength reduces along the cross-sectional area of the magnet, reducing the total force production when the coil is in motion. Therefore, we selected a gap of 400 µm to maximize the field intensity. We chose a horizontal separation between the magnet pairs of 1 mm to maximize coil displacement during operation.

Using the parameters from our magnetic core, the lift coil is constrained to the following dimensions: width ($w = 3$ mm), length ($l = 3 - 5$ mm), and height ($h = 0.3$ mm), as shown in Fig. 4. The wire thickness (t) informs both the number of turns (N) and the total coil resistance (R). To maximize force output, we want to maximize the number of turns while minimizing resistance (and therefore resistive losses). We simulated a number of wire thicknesses, corresponding to $40 - 48$ AWG magnet wire within a fixed cross sectional area of 0.3 mm^2. As can be seen in Fig. 5, as the number of turns increases for a fixed area, the output force linearly increases, as we expect from Eq. 1. We performed similar analysis to size the magnetic core and coil parameters for the swing actuator.

B. Fabrication and Assembly

The final actuator assembly is shown in Fig. 6(a). We first assemble the magnetic core by laser cutting 100 µm Hiperco sheets (Hiperco 50A, Vulcan Metal Group) to the appropriate dimensions (5.5×3 mm^2) and then we align and attach each permanent magnet using cyanoacrylate (CA) adhesive (Loctite 495). We then assembled the polyimide spacer layers (500 µm) that were prepatterned in the laser cutter and then adhered to the Hiperco with CA glue (see Fig. 6(b)). To fabricate the coils (shown in Fig. 6(c)), we designed an alignment jig to maintain the inner and outer

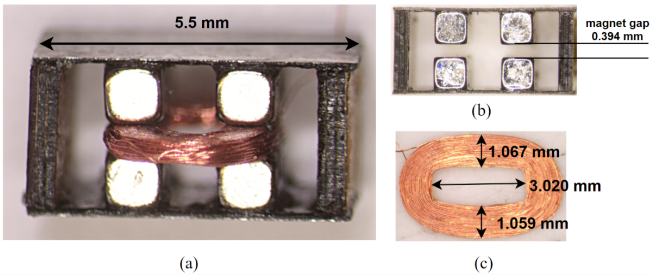

Fig. 6: Manufactured VCA (a) Front view of actuator with coil in neutral position. Magnets are glued to alloy backing and polyimide spacers hold the structure apart. (b) Magnet gap of 0.384 mm. (c) Top view of coil dimensions. The widths are relatively similar to that of the magnet dimensions, maximizing the current density within the gap.

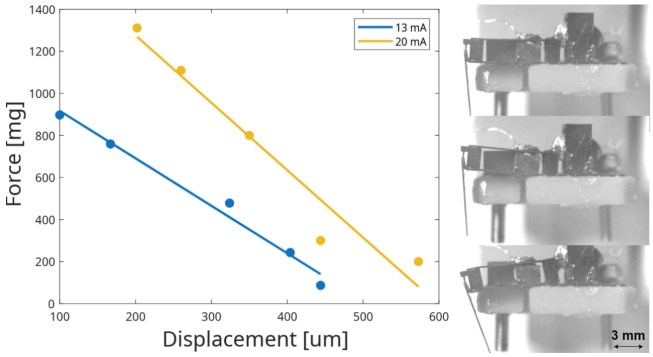

Fig. 7: Linear relationship between force and displacement in the planar VCAs. Representative example of data was collected with actuator attached to the lift parallelogram at 13 mA and 20 mA.

radii, then we hand wound 48 AWG self-bonding magnet wire (46653, MWS Wire). We selected 48 AWG wire with $N = 190$ for the lift actuator and $N = 220$ for the swing actuator.

C. Experimental Validation

To validate VCA performance, we measured blocked force using a high-resolution force sensor (Nano17Ti, ATI Industrial Automation). We varied number of turns, wire gauge, and current to compare experimental results with the simulation in Fig. 5. Because the coil moves within the magnetic core, we attached a rigid carbon fiber beam that extends beyond the core to reliably contact the sensor. As can be seen in Fig. 5, the experimental results show good agreement with the ANSYS simulations, with an average absolute error of 32 mg. Measured forces deviate from expected values at higher currents and thinner wire gauges due to heating and resistive losses. To confirm linear performance [20] in the actuator-leg system, we mounted the lift actuator into a single-leg mechanism and recorded force over varying actuator displacements. As the coil moves between the permanent magnets, the number of turns (N) in the magnetic field decreases. This effect can be seen in Fig. 7, where the force decreases linearly with displacement.

IV. Assembled Robot

We manufactured four single-leg mechanisms using the fabrication method described in Sect. II. We then attached each leg to a carbon fiber chassis (111 µm, M55J, TorayCA), which served as the mechanical ground for the entire structure. With the four legs attached, we then inserted the actuators into each leg, first attaching the magnetic core to mechanical ground and then the coils to the leg linkages using CA glue. The final leg design has a lift transmission ratio (A:B) of 1:3 and a swing transmission ratio (C:D) of 1:2.5. We found that this provided a leg displacement greater than 1 mm and a leg force greater than 500 mg to support the weight of the robot. The fully-assembled robot is shown in Fig. 1, and the mass of each mechanical component is shown in Table I.

TABLE I: COMT Mass Distribution

Component	Mass [mg]
Leg Transmissions	540
Chassis	119
4 Lift Actuators	368
4 Swing Actuators	143
8 coils	80
Total Mass	1250

A. Leg Phasing

Leg phasing has been extensively investigated to identify strategies that balance stability, speed, and efficiency across a wide range of scales [21], [22]. Interleg phasing (ϕ_g) between contralateral and ipsilateral legs enables robots to coordinate support for gaits such as walking, trotting, or bounding. Intraleg phasing (ϕ_p) between the lift and swing DOFs dictates the timing of ground contact relative to forward motion [21]. Figure 8 shows a 90° baseline phase offset (ϕ_b) between lift and swing actuation signals in a single leg, which results in a rectangular foot trajectory. If we couple the front left and back right leg actuation signals and employ an interleg phase offset with the opposing diagonals ($\phi_g = 180°$), we achieve a trot gait with alternating rectangular foot trajectories (see Fig. 9).

To control robot orientation, we vary the intraleg phasing between the lift and swing actuators on the left side of the robot by ϕ_t, such that $\phi_p = \phi_b + \phi_t$ [23]. To visualize this, we drew the actuation signals for all four legs in Fig. 10. The interleg phasing ϕ_g remains constant: the lift signal for the front left leg and back right leg match and have a 180°

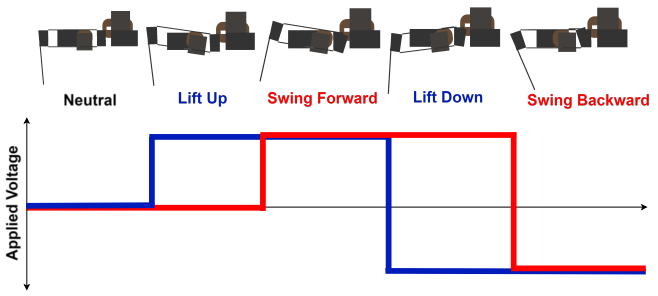

Fig. 8: A 90° phase offset between lift and swing actuator signals demonstrates rectangular-like motion of leg tip. Swing is actuated in different directions at alternating times compared to lift.

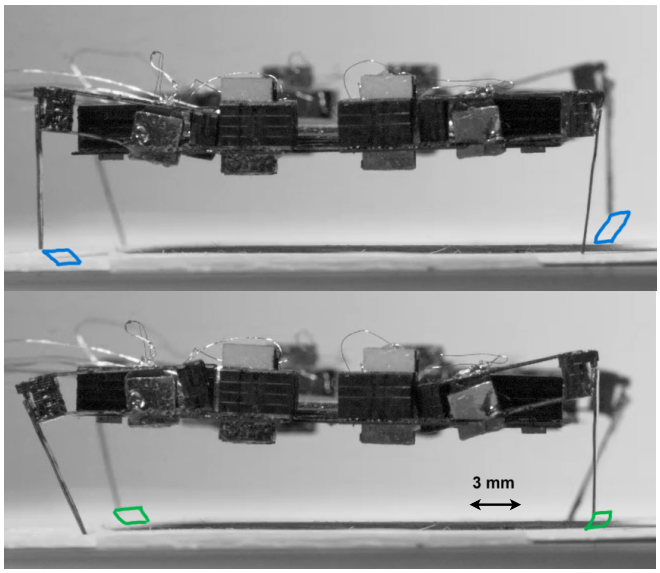

Fig. 9: Trot leg tip trajectory produces alternating across one diagonal (blue) and then the complementary diagonal (green). Variation in lift and swing displacement may contribute to asymmetric turning.

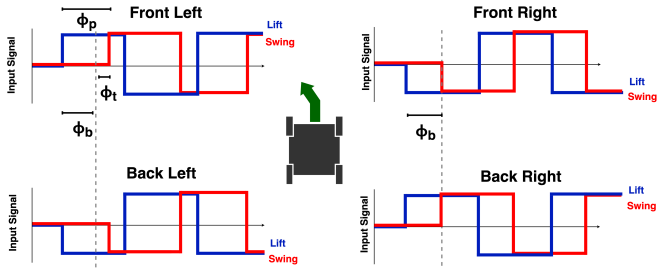

Fig. 10: A left turn is induced with positive ϕ_t in a trot.

phase offset with the front right leg and back left leg. The left swing signals are delayed by ϕ_t relative to the baseline phase offset (ϕ_b) present in all swing signals. This additional delay shortens the time that the left side is both down and pushing back, leading to larger swing force on the right side of the body. The robot therefore turns to the to the left (or counter-clockwise). If we induce a negative turning phase ($-\phi_t$) the robot will turn right (or clockwise).

Thus, instead of generating eight independent control signals, we can generate straight-line and turning trajectories with four independent control signals (left lift, right lift, left swing, right swing). Because we keep interleg phasing constant, we can switch the current direction on the front right and back left coils relative to the front left orientation. For this simple control strategy, our electrical system requires four independent general-purpose input-output (GPIOs) signals or pulse-width-modulated (PWM) signals, as well as motor drivers to amplify the current and control current direction. We leave more detailed gait analysis to future work.

B. Electrical System

Our at-scale electrical system can be seen in Fig. 11. The printed circuit board (PCB) contains a microcontroller unit (MCU, KL46, NXP Kinetis), two motor drivers (DRV8833C), an inertial measurement unit (ICM-42688-P), a power switch, and a low-dropout voltage regulator (TPS7A0333DQNR) to control the voltage input to the IMU and MCU. The IMU is not used in this work, but was integrated for future closed-loop operation. For short untethered tests, we used a 385 mg Lithium-ion battery (Powerstream, PGEB201212C). Each component was selected to meet the payload requirements of the vehicle, and the PCB adds an additional 292 mg for a total untethered system mass of 1.9 g.

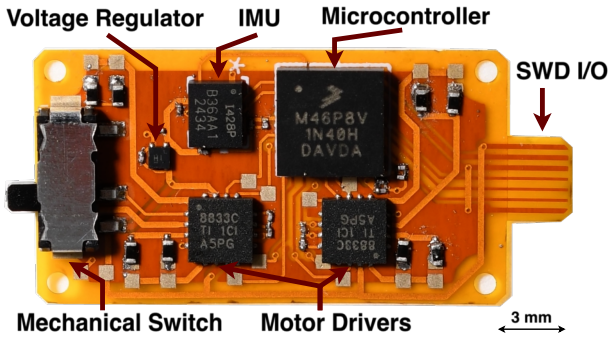

Fig. 11: Printed Circuit Board

V. Robot Performance

We first conducted full-body simulations of the electromagnetic crawling robot in MATLAB Simscape Multibody to analyze the natural frequencies of the swing and lift parallelograms, and the chassis. Mechanical resonance of the actuator alone was experimentally determined to be approximately 200 Hz. Leg timing is critical to optimize performance, enhancing stride length and ground reaction forces. Operating near body resonance (31 Hz) can enable faster operation, as body oscillation can reduce the effective mass on the actuators. Conversely, operating near the resonant frequency of the lift or swing parallelograms, can produce more ineffective stances [24], as the leg will oscillate out of phase with the actuation signal. We experimentally measured the robot's natural frequency by inducing free oscillations in the respective DOF and recording the response using high-speed videography (Phantom VEO 710). The results are shown in the Table below. We see consistency in the lift parallelogram and body modes, with slight deviation in the swing parallelogram. We believe that this is due to unmodeled stiffness in the swing hinges.

TABLE II: Mechanism Resonant Frequencies

Mechanism	Simulated	Experimental
Lift Parallelogram	130 Hz	147 Hz
Swing Parallelogram	488.7 Hz	330 Hz
Body	31.5 Hz	31 Hz

A. Straight-Line Trajectories

We tested the trot gait across multiple frequencies (20 – 80 Hz) and on multiple surfaces (cardstock, rubber, 400-grit sandpaper and 3000-grit sandpaper) and recorded the

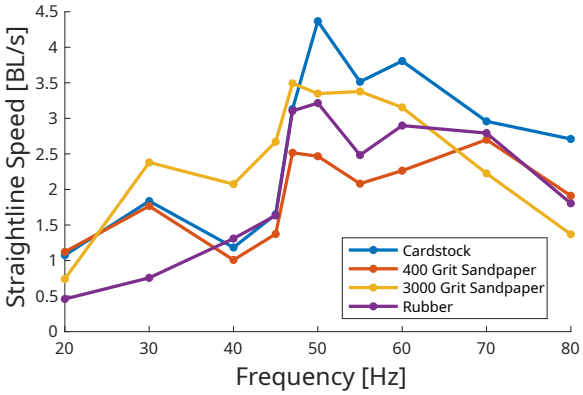

Fig. 12: Trot speed versus gait frequency on cardstock, 400 grit sandpaper, 3000 grit sandpaper, and rubber. Similar speed profiles are seen across different materials and are indicative of resonant peak at $45 - 50Hz$

untethered speed of the robot. As can be seen in Fig. 12, COMT reaches its maximum speed at 50 Hz across all materials, with a fastest recorded speed of 4.36 BL/s (BL = 3 cm). We see a noticeable first peak at $\sim$ 30 Hz, which corresponds to the increased performance at body resonance. The second peak at 50 Hz is the system resonance, which couples the ground interaction effects on the body, leg, and actuator during operation. Notably, the robot is able to move at higher speeds on smooth surfaces, such as cardstock and fine-grit sandpaper. On the coarser sandpaper, the robot is not able to move effectively with increased surface roughness. Therefore, in future autonomous operations where the robot will encounter more varied substrates, we need to increase the lift transmission ratio or employ different gait strategies to overcome larger obstacles.

B. Turning Performance

Using the leg phasing techniques described in the previous section, we varied $\phi_t = [-60, -50, -40, 0, 40, 60]$ and recorded the tethered robot position in the $x - y$ plane as well as the heading angle using high-speed video. All turning experiments were performed at a driving frequency of 50 Hz after it was determined to be the fastest straight-line frequency. Achieved angular speeds ranged from $6 - 63$ °/s (Fig. 13). The robot used in these experiments had a pronounced difference between the left and right sides, which led to a noticeable left turn with zero phase offset. As seen in Fig 13, we commanded a $\phi_t = -60°$ phase offset to achieve straight-line trajectories. While the robot did not make significant forward progress during right turns, we can see that the robot was able to maintain a consistent change in heading angle across all commanded turns (see Fig. 13). Additionally, Fig. 14 shows the robot performing a tight right turn in place.

C. Robot Efficiency

We recorded the current consumption of the actuators during tethered robot testing. While we expected each actuator to consume $\sim$ 20 mA given our body mass, we found that each actuator drew approximately 46 mA. We hypothesize

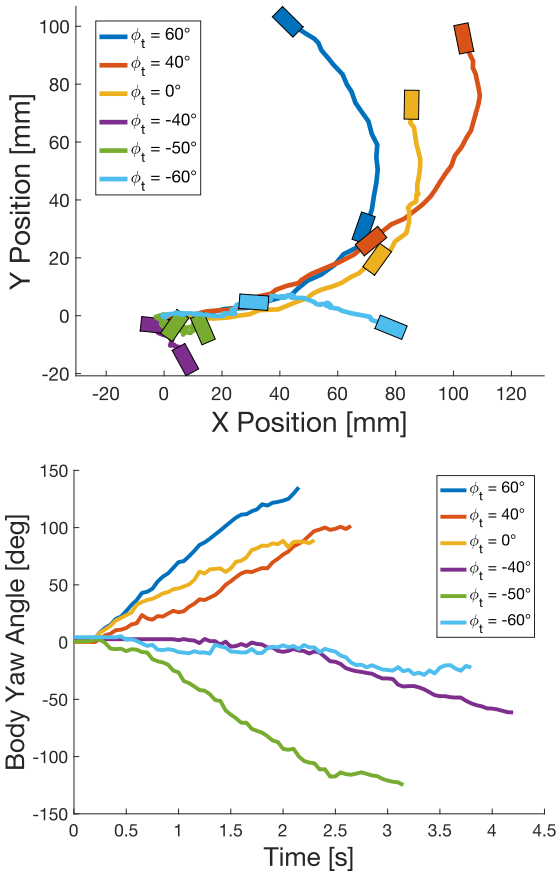

Fig. 13: Open-loop maneuverability under varied phase offsets (ϕ_t) on cardstock. The $x - y$ position of the robot is shown on the top, with the measured body angle from the same experiments shown on the bottom.

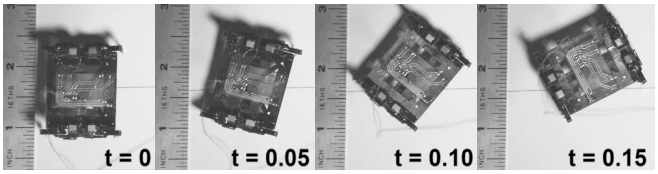

Fig. 14: A sharp right turn in place with $\phi_t = -50°$ is achieved within 0.16 s.

that this discrepancy is due to heating and resistive losses in the actuator, indicating that future designs should use higher gauge wire in the coils. However, at 368 mA, the total current consumption is less than other electromagnetic insect-scale robots [10], [11] and generates higher straight-line speeds.

VI. Conclusion

We developed COMT, an insect-scale crawling robot that utilizes planar electromagnetic actuators to locomote. By tuning inter- and intra- leg phasing, we were able to demonstrate open-loop straight-line and turning trajectories. Using coupled signals, we built low-mass electronics and integrated them onboard a 1.9 g robot. The simplified fabrication strategy allows for minimal human intervention and enables future mass production. While it is not as efficient as similarly-sized piezo-driven robots [1], COMT

shows comparable performance to other electromagnetic designs. We will improve actuator performance, looking into designs with thicker wire gauges to reduce resistive losses. Using PWM signals can increase current for fractions of a second to increase force and displacement of the actuator without increasing power consumption. While each leg is currently hand-assembled onto the chassis, future iterations can include the PCB and chassis as embedded layers in the fabrication process, further reducing manual intervention steps. This work lays the foundation for mass-assembled insect-scale robots with sufficient maneuverability to travel over unstructured environments.

ACKNOWLEDGMENT

This work was sponsored in part by the Office of Naval Research (N00014-24-1-2141-P00001). Any opinions, findings, and conclusions or recommendations expressed in this material are those of the author(s) and do not necessarily reflect the views of the Office of Naval Research. The authors would like to thank fellow lab members Hang Gao, Cameron Urban, and Cheney Zhang for their valuable insights.

REFERENCES

[1] R. S. Pierre and S. Bergbreiter, "Toward autonomy in sub-gram terrestrial robots," *Annual Review of Control, Robotics, and Autonomous Systems*, vol. 2, no. 1, pp. 231–252, 2019.

[2] J. P. Whitney, P. S. Sreetharan, K. Y. Ma, and R. J. Wood, "Pop-up book mems," *Journal of Micromechanics and Microengineering*, vol. 21, no. 11, p. 115021, oct 2011.

[3] F. R. S. et al., "Considerations for the design and rapid manufacturing of pop-up mems devices," *Advanced Materials Technologies*, 2024.

[4] B. G. et al., "Power and control autonomy for high-speed locomotion with an insect-scale legged robot," *IEEE Robotics and Automation Letters*, vol. 3, no. 2, pp. 987–993, apr 2018.

[5] H. Kabutz, A. Hedrick, W. P. McDonnell, and K. Jayaram, "mclari: A shape-morphing insect-scale robot capable of omnidirectional terrain-adaptive locomotion in laterally confined spaces," in *2023 IEEE/RSJ International Conference on Intelligent Robots and Systems (IROS)*, 2023, pp. 8371–8376.

[6] H. Hussein, A. Damdam, L. Ren, Y. O. Charrouf, J. Challita, M. Zwain, and H. Fariborzi, "Actuation of mobile microbots: A review," *Advanced Intelligent Systems*, vol. 5, no. 9, p. 2300168, 2023.

[7] R. J. W. M. Karpelson, G. Wei, "Driving high voltage piezoelectric actuators in microrobotic applications," *Sensors and Actuators A:Physical*, vol. 176, pp. 78–89, April 2012.

[8] Z. Zhakypov, K. Mori, K. Hosoda, and J. Paik, "Designing minimal and scalable insect-inspired multi-locomotion millirobots," *Nature*, vol. 571, no. 7765, pp. 381–386, Jul. 2019.

[9] X. Yang, L. Chang, and N. O. Pérez-Arancibia, "An 88-milligram insect-scale autonomous crawling robot driven by a catalytic artificial muscle," *Sci. Robot.*, vol. 5, no. 45, p. eaba0015, Aug. 2020.

[10] W. Langford and N. Gershenfeld, "Discretely assembled walking machines," *Journal of Micro-Bio Robotics*, vol. 16, pp. 13–22, 2020.

[11] Z. Liu, W. Zhan, and X. L. et al., "A wireless controlled robotic insect with ultrafast untethered running speeds," *Nature Communications*, vol. 15, p. 3815, 2024.

[12] P. Bhushan and C. Tomlin, "An insect-scale self-sufficient rolling microrobot," *IEEE Robotics and Automation Letters*, vol. 5, no. 1, pp. 167–172, jan 2020.

[13] R. Malka, A. L. Desbiens, Y. Chen, and R. J. Wood, "Principles of microscale flexure hinge design for enhanced endurance," in *2014 IEEE/RSJ International Conference on Intelligent Robots and Systems*, Chicago, IL, USA, 2014, pp. 2879–2885.

[14] P. Bhushan and C. Tomlin, "Design of the first sub-milligram flapping wing aerial vehicle," 2019, arXiv:1908.03203.

[15] P. Bhushan and C. Tomlin, "Design of an electromagnetic actuator for an insect-scale spinning-wing robot," *IEEE Robotics and Automation Letters*, vol. 5, no. 3, pp. 4188–4193, jul 2020.

[16] M. Pakkratok, N. Luekiatphaisan, and H. Aoyama, "Combination of vca based micro force generator and micro robot for micro hardness and stiffness test," in *Proceedings of SICE Annual Conference 2010*, Taipei, Taiwan, 2010, pp. 3184–3189.

[17] R. M. McKenzie, M. E. Sayed, M. P. Nemitz, B. W. Flynn, and A. A. Stokes, "Linbots: Soft modular robots utilizing voice coils," *Soft Robotics*, vol. 6, no. 2, pp. 195–205, 2019.

[18] W. Zhou and S. Huang, "An accurate model for fast calculating the resonant frequency of an irregular solenoid," *IEEE Transactions on Microwave Theory and Techniques*, vol. 67, no. 7, pp. 2663–2673, jul 2019.

[19] J. L. G. Janssen, J. J. H. Paulides, L. Encica, and E. Lomonova, "High-performance moving-coil actuators with double-sided pm arrays: A design comparison," in *2010 International Conference on Electrical Machines and Systems*, Incheon, Korea, 2010, pp. 1657–1660.

[20] N. Anandan, A. Varma Muppala, and B. George, "A flexible, planar-coil-based sensor for through-shaft angle sensing," *IEEE Sensors Journal*, vol. 18, no. 24, pp. 10 217–10 224, 2018.

[21] N. Doshi, K. Jayaram, B. Goldberg, and R. J. Wood, "Phase control for a legged microrobot operating at resonance," in *2017 IEEE International Conference on Robotics and Automation (ICRA)*, 2017, pp. 5969–5975.

[22] Y. Fan, Z. Pei, C. Wang, M. Li, Z. Tang, and Q. Liu, "A review of quadruped robots: Structure, control, and autonomous motion," *Advanced Intelligent Systems*, vol. 6, no. 6, p. 2300783, 2024.

[23] B. Goldberg, N. Doshi, and R. J. Wood, "High speed trajectory control using an experimental maneuverability model for an insect-scale legged robot," in *2017 IEEE International Conference on Robotics and Automation (ICRA)*, Singapore, 2017, pp. 3538–3545.

[24] B. Goldberg, N. Doshi, K. Jayaram, and R. J. Wood, "Gait studies for a quadrupedal microrobot reveal contrasting running templates in two frequency regimes," *Bioinspiration and Biomimetics*, vol. 12, no. 4, 2017.